CrossMark

Finite Strain Kinematics of Multi-scale Material by Digital Image Correlation

Jérémy Marty[1] · Julien Réthoré[1] · Alain Combescure[1] · Philippe Chaudet[1]

Abstract In this study, we present a method to analyse experimentally the deformation kinematics of a heterogeneous material using digital image correlation. The periodicity of the microscopic deformation patterns is assessed from the displacement measured along the edges of unit cells. The first order macroscopic transformation gradient is shown to enable capturing the deformation of the unit cell even for large plastic strains. It is also shown that cells along the boundary of the heterogeneous media have a non periodic higher order kinematics.

Keywords Large strain · Multi-scale material · Digital image correlation · Homogenization

Introduction

Materials, even more natural materials, are heterogeneous at a certain observation scale. Homogenization techniques which consist in the prediction of the properties at the macroscopic scale directly from the properties of the microstructure (geometries, phases and behaviours) are efficient to predict the effective elastic properties of heterogeneous materials [1]. In presence of geometrically and physically nonlinear phenomena, it is clearly more difficult [2, 3].

✉ Julien Réthoré
julien.rethore@insa-lyon.fr

Jérémy Marty
jeremy.marty@insa-lyon.fr

[1] Laboratoire de Mécanique des Contacts et des Strcutures INSA Lyon / UMR CNRS 5259, 20 Avenue des Sciences F-69621 Villeurbanne Cedex, France

For many methods large deformation cannot easily be taken into account because of the non linearities, for instance evolution of the microstructure or strain localization which often appear.

As an alternative, multi-scale methods, as for example the FE^2 technique, brings new perspectives to obtain detailed information for structures with two scales [4, 5]. Contrary to homogenization techniques, the material behaviour is enforced at the microscopic scale and the macroscopic scale enforces the balance of the homogenized stresses. The FE^2 method consists in two nested finite element problems with one Representative Volume Element (RVE) at each integration point of the macroscopic problem. This method is efficient for small strain but in presence of large strain and failure, issues about the choice and the existence of the RVE appear as presented by Gitman [6]. This definition may not be reached when strongly non-linear process or failure occurs at the macroscopic scale. This is why some authors like Kouznetsova, Feyel, Forest or Kaczmarczyk [7–10] use the theory of second gradient or Cosserat continuum to model the macroscopic scale whereas the microscopic continuum remains classical. Theoretically, this improvement allows for taking into account large strain and rotations of both scales with better accuracy. Moreover the absolute scale separation is no more required when the macroscopic deformation gradient and its gradient are used to determine the boundary conditions applied to the microscopic scale.

For now, the multiscale methods are in general validated by comparison with *full field* simulations. Multiscale experimental methodologies based on digital image correlation have recently appeared. The ductile failure of an aluminium is studied by Ghahremaninezhad [11] with displacement field measurements at the macroscopic scale while microscopy are realised *post-mortem* to get the real

strain to failure of the heterogeneity. Passieux in [12] use two cameras to locally improve the resolution of the measured macroscopic strain when it is needed by the microstructure. The evolution of an architectured material has been studied and analysed by Weck in [13] on thin metallic sheets containing a significant number of laser drilled holes. Tension tests have been carried out in a scanning electron microscope but displacement field measurements are not performed.

However, these techniques do not provide experimental data that could be exploited for the analysis of scale transition schemes. In the papers listed above, the analysis at the two scales are partially or even fully uncoupled. The relationships between the kinematic fields at the two scales cannot be investigated. There is thus a need for dedicated experiments and post-processing techniques to analyze quantitatively the deformation of multiscale materials at two separate scales, the main difficulty being to obtain the displacement fields at the two scales over the same region of the sample. These data should allow for investigating the relationships between the measurements at these two scales in the linear as well as in the non-linear regime. While there are strong theoretical bases concerning these relations in the elastic regime, the non-linear regime with large plastic strains is much more difficult to study theoretically and numerically. The usefulness of experimental data obtained in this context is even more important.

This paper presents a multiscale structure which is loaded in uniaxial tension to measure experimentally the kinematics of the RVE's deformation. The structure is a stainless steel sheet which has been perforated to construct a heterogeneous material. One unit cell is composed of a square with a hole at the center. The number of unit cells is about 1900. As it will be shown, an efficient scale separation is obtained. A high resolution camera (with a captor of 29 million pixels) is used to take pictures along the deformation process. The displacement fields are measured and strain fields are deducted with Digital Image Correlation (DIC) techniques [14, 15]. This high resolution allows to perform full field measurements at both scales of the structure (the macroscopic as well as the microscopic one). Different orientations of the unit cell keeping a fixed macroscopic loading direction produce different solicitations into the microstructure : uniaxial tension as well as mixed tension and shear loadings. The aim of the paper is to produce experimental data which allows to ensure or to invalidate the usual hypothesis of two scale models and also to evaluate the regions of the multiscale structure for which the use of a second gradient approach is required. The linear regime as well as the non-linear regime with large plastic strain will be investigated.

The paper is organized as follows, in section "Digital Image Correlation" the principle of DIC and the proposed improvement for analysing the large strain ultra-high resolution images are presented. Section "Experiments" describes the experimental setup and the results of DIC at macroscopic and microscopic scales. These results, in terms of displacement fields, are then analysed in section "Unit Cell Kinematics".

Digital Image Correlation

General Settings and Notations

DIC is a full field measurement method which enables to capture the displacement field at the surface of a structure. This method is based on the grey level conservation between two images. Let us call the reference image f and the deformed image g. The grey level of the two images is supposed to be passively advected to find the displacement field $\mathbf{v}$ at each pixel $\mathbf{x}$:

$$f(\mathbf{x}) = g(\mathbf{x} + \mathbf{v}(\mathbf{x})) - b(\mathbf{x}), \tag{1}$$

where b is the noise appearing between the images. The best approximation of the displacement $\mathbf{v}$ is obtained by assuming there is no noise, this approximation is called $\mathbf{u}$. To determine $\mathbf{u}$ one can solve this ill-posed inverse non-linear problem over the region of interest (ROI) by minimizing the least-squares functional ϕ^2:

$$\phi^2(\mathbf{u}) = \int_{ROI} [f(\mathbf{x}) - g(\mathbf{x} + \mathbf{u}(\mathbf{x}))]^2 d\mathbf{x}. \tag{2}$$

Following Besnard [15], we adopt a Finite Element discretization for the displacement field. The discretized displacement field reads:

$$\mathbf{u}(\mathbf{x}) = \sum_{i \in N} \mathbf{u_i} \underline{N}_i(\mathbf{x}) = \underline{\underline{N}} \mathbf{U}, \tag{3}$$

where $\mathbf{u}_i$ is the set of finite element degrees of freedom (DOFs), and $\underline{N}_i$ the finite element shape functions associated with the finite element mesh. A matrix form of this equation is used: $\underline{N}$ is a matrix that collects the values of the N vector shape functions at a given location $\mathbf{x}$ and $\mathbf{U}$ the vector that collects the values of the displacement DOFs. Note that $\underline{N}$ has N columns and as many lines as points where the shape functions are evaluated. For clarity, the positions of these evaluation points are omitted in the matrix format.

Using a first order Taylor expansion, the functional ϕ^2 becomes a quadratic form of solution increments $d\mathbf{u}$. The minimization thus leads to a sequence of linear systems written:

$$\left[\int_{ROI} [(\nabla g(\mathbf{x} + \mathbf{u}).\underline{N}_j(\mathbf{x}))]^T (\nabla g(\mathbf{x} + \mathbf{u}).\underline{N}_i(\mathbf{x})) d\mathbf{x} \right] du_i$$
$$= \int_{ROI} [f(\mathbf{x}) - g(\mathbf{x} + \mathbf{u})(\nabla g(\mathbf{x} + \mathbf{u}).\underline{N}_j(\mathbf{x}))] d\mathbf{x}, \tag{4}$$

where ∇ denotes spatial derivation. This minimization is equivalent in a matrix form as:

$$M_{ji}.du_i = F_j. \tag{5}$$

In this equation, M_{ji}, respectively F_j and du_i, denotes the component of the matrix, respectively right hand side vector and displacement increment vector, of the resulting linear system to solve. Other authors propose specific basis function like Hild [16] for cantiliver beam kinematics or Réthoré [17] with NURBS functions. Once the convergence is reached, the calculated displacement field **u** is reconstructed over the ROI. The correlation error is obtained by comparing the reference image f to the deformed image g advected with the displacement **u**:

$$\eta = |g(\mathbf{x} + \mathbf{u}(\mathbf{x})) - f(\mathbf{x})|. \tag{6}$$

Large Strain Resolution

During the experiments, strongly heterogeneous strain fields have to be captured. They are due to the strain concentration resulting from the geometry of the model microstructure. Moreover the material has a ductile behaviour and very large strain are obtained in the vicinity of the microstructural holes. When the deformation of one element becomes large and/or when erratic deformation due to noise measurement occurs, the element is distorted and convergence of the DIC is lost around this element. To avoid this phenomena, the gradient of the deformation of the elements is artificially limited by adding locally (at the element level) a Tikhonov regularization [18]. It consists in adding to the element correlation matrix M_{ij}^{el} a contribution of the following form:

$$R_{ji}^{el} = \int_{el} (\nabla \underline{\underline{N}}_j(\mathbf{x})) : (\nabla \underline{\underline{N}}_i(\mathbf{x})) d\mathbf{x} \tag{7}$$

This regularization term is then appropriately weighted (compared to M_{ij}^{el}) so that the wave length of the displacement fluctuation is locally limited to a given length l_c (see [19] for a description of this formalism). In practice, this cut-off wave length l_c is set to the unit cell size. Consequently, the amount of regularization is very limited and as it is introduced locally, it does not introduce an artificial global smoothing of the strain field. It just allows for maintaining convergence of the DIC alogorithm while large element distortion are measured. Indeed, the criterion for introducing the local regularization is that the determinant of the Jacobian matrix of the element in the deformed configuration becomes negative at one Gauss point. The regularization enforces that the deformed elements keep a geometrically admissible shape thus avoiding local convergence problem. Note that if an element is regularized at a given step of the analysis then the regularization is maintained up to the end of the analysis. This strategy allows to avoid local convergence problem when strongly heterogeneous strain fields are searched for without artificial global smoothing of the local variation of the displacement and strain fields.

Experiments

Model Material

The tested structure is a plate, 1 *mm* thick, with holes distributed on a square grid delimited by a circle of 49 holes in diameter at the specimen center : the total number of holes is about 1950. The holes diameter is 0.5 *mm* whereas the distance between their center, the grid step, is 1 *mm*. The structure of the architectured material is presented in Fig. 1(a) and is loaded in a tensile machine. The dimensions of the entire specimen are given in Fig. 1(c), the width and the length of the specimen being equal to 89 mm and 98 mm respectively. The plate thickness being small compared to the in plane dimensions, a plane stress assumption holds at the macroscopic scale. However this hypothesis can be discussed locally as the holes diameter is half of the plate thickness. The bulk material is a 304L stainless steel which has a known elastic-plastic constitutive behaviour. The behaviour of the material has been identified by Réthoré [20] with DIC experiments. For the elastic regime, the parameters are Young's modulus E and Poisson's ratio ν which values are set to 198 GPa and 0.25, respectively. For the plastic regime, a non-linear isotropic hardening is considered. The evolution of the yield stress σ_Y as a function of the accumulated plastic strain ε_p is parametrized as follows:

$$\sigma_Y(\varepsilon_p) = H\varepsilon_p + S_Y \left(1 + \frac{\varepsilon_p}{\varepsilon_0}\right)^{\delta}, \tag{8}$$

H being a linear hardening coefficient, S_Y the initial yield stress, ε_0 a scaling factor for the accumulated plastic strain and δ the hardening exponent. These parameters are set to 1480 MPa, 284 MPa, 10^{-5} and 0.042 respectively.

Three different samples have been studied in this work to load the heterogeneous zone in mixed loadings of tension and shear. In addition to the sample described by Fig. 1(a), two samples with a 30° and 45° hole network inclination have been tested. The reference image of the non inclined plate is also shown in the Fig. 1(b). To understand the rotation of the network, zooms of reference images of the three samples are shown in the Fig. 2.

In these two cases, a typical unit cell (a square with a hole) is loaded with both tension and shear. The experimental equipment to obtain the digital images is a high resolution camera of 6576 × 4384 pixels -29 millions of pixels- (Camera Vieworks : VN-29MC-M5A0-FM) mounted with a 200 *mm* lens (Schneider Xenon Emerald). Thanks to this

Fig. 1 (**a**) Geometry and boundary conditions. (**b**) Reference image and (**c**) technical drawing of the sample microstructure oriented at 0°
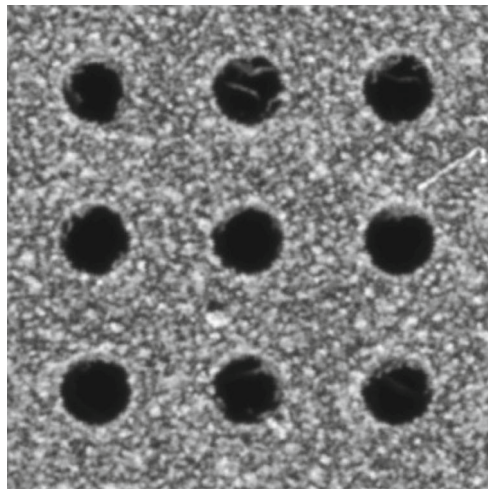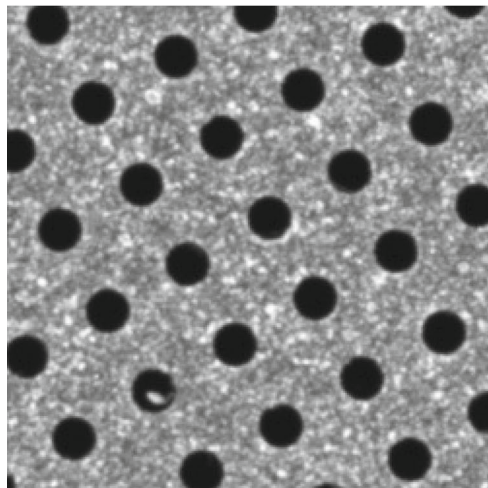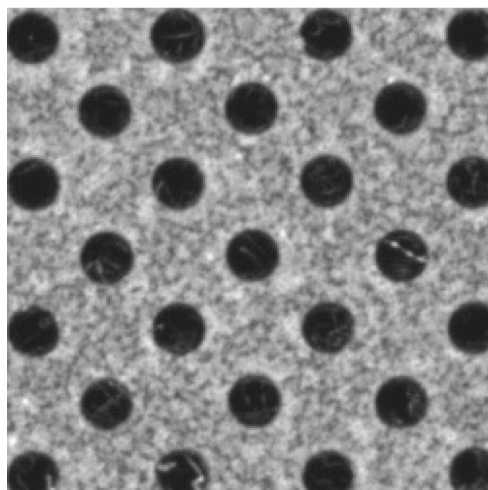

(a)

(b)

(c)

(a) 0° case

(b) 30° case
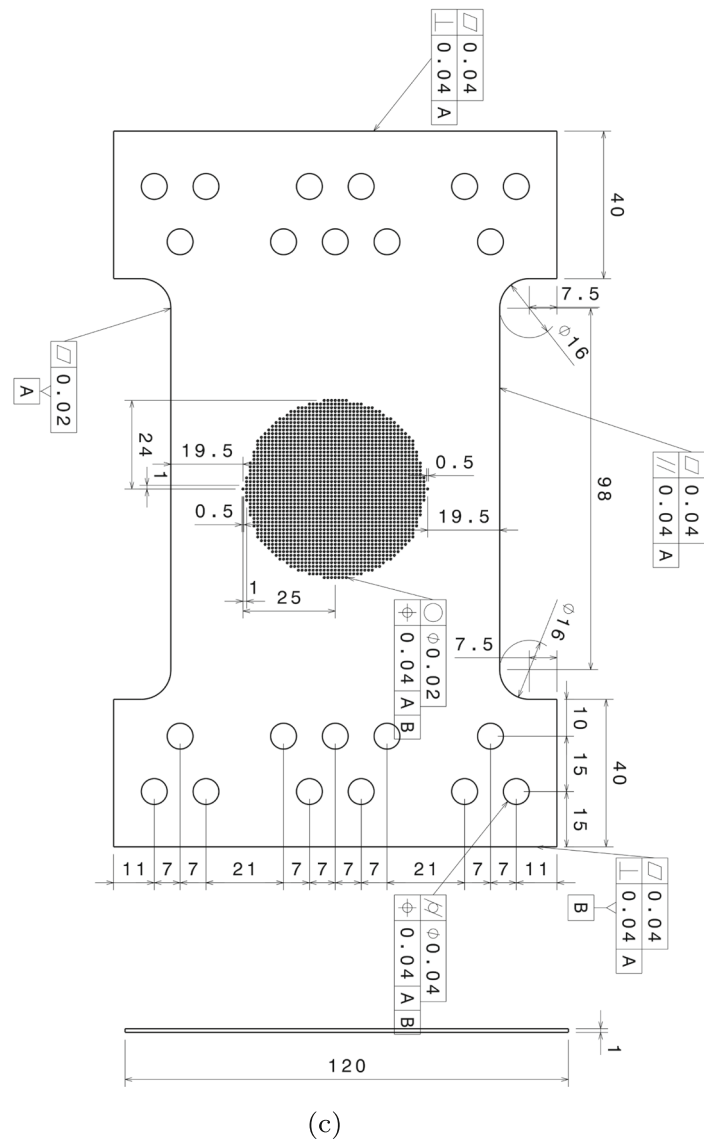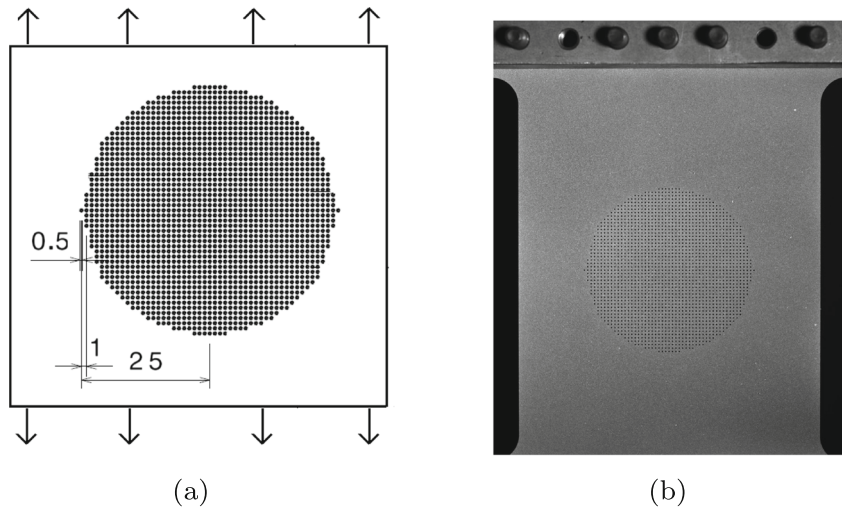
(c) 45° case

Fig. 2 Close view of the hole lattice for the three different orientations: 0, 30 and 45°

high resolution device, we can perform DIC analysis at the macroscopic scale as well as at the microscopic scale over the whole sample surface. For the macroscopic scale, a structured mesh of quadrangular square elements is used. The mesh is constructed so that each element corresponds to a unit cell of the hole network. Two unit cells of homogeneous material are added around the architectured material to form the entire macroscopic mesh. For the microscopic scale, an unstructured mesh of the unit cell is built (see Fig. 3(b)). This unit cell mesh is then replicated over the grid so that the microstructure region is entirely described (plus two cells of the homogeneous material with a compatible mesh). With the optical setup used in the experiments, the unit cell size is 50 pixels. The pixel spatial resolution is then equal to 0.02 mm per pixel. The unit cell mesh being constructed with 8 nodes per side the approximate element size is 7 pixels. These meshes are presented in Fig. 3.

Macroscopic Responses

The load versus displacement curves are displayed in Fig. 4 for the three experiments. The displacement rate is set to 0.1 *mm* per minute within an elongation range equal to twice linear regime and then 1 *mm* per minute. To avoid image bluring, the mechanical loading is stopped each time an image is acquired. The displacement is maintained and the force decreases due to relaxation. This produces vertical lines in the load displacement curves represented in Fig. 4. For the 0 degree case, a tensile mode is promoted whereas 30° and 45° cases enable shear modes to develop. This results, for the latter cases, in higher displacement (in the macroscopic loading direction) to failure.

Strain Fields Measured by DIC

Strain fields measured at the macroscopic scale are plotted in Fig. 5 for the three experiments. The same average strain (corresponding to the vertical elongation) of the architectured material is considered for the three cases and is equal to 20 %. The value of the Von Mises strain field is plotted. The architectured material has a higher strain than the homogeneous material, it is due to the hole inside the unit cell which concentrates the strain. The macroscopic kinematic is not able to capture the microscopic effects inside the unit cells, the strain field is almost homogeneous over the whole architectured material.

A close view of measured microscopic strain fields are plotted in Fig. 6 for the zone represented inside the dashed rectangle of the macroscopic field (Fig. 5). The value of the Von Mises strain field is again plotted. The kinematic at the microscopic scale is captured. For the three experiments the strain concentration occur around the hole, it is due to

Fig. 3 Meshes for the macroscopic (*left*) and the microscopic (*right*) correlation analysis

(a) (b)
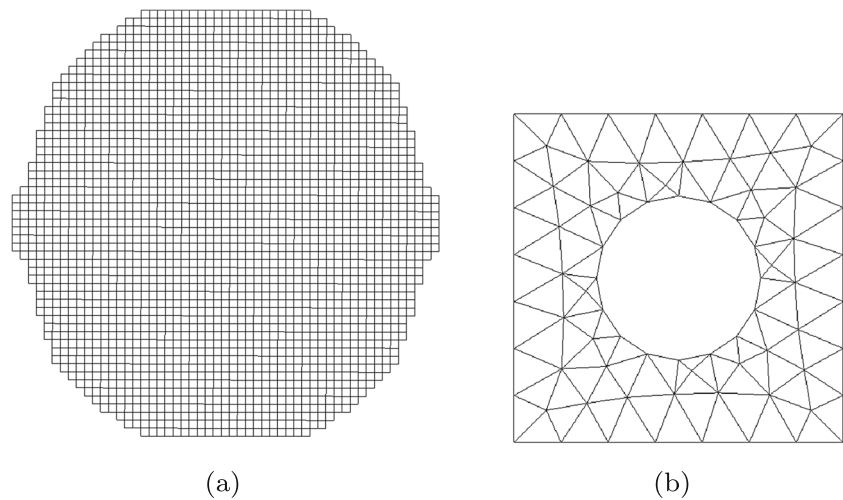
the repetition of the unit cell geometry. For each experiment, the strain distribution patterns seem to have very small variations between the cells that are not on the boundary of the architectured material.

For the 0 degree case (Fig. 6(a)), a shielding effect is obtained: the strain is lower in the region between the holes located over vertical lines (the holes shield the global loading). On the contrary, higher strain level are obtained over ligaments where shielding by the holes does not occur. One observes that the most deformed unit cells are located on both ends of the horizontal middle line of the architectured zone. This will lead to crack initiation at this position. The crack will then propagate towards the center of the plate and finally through the homogeneous zone toward the sample edges. In these two extreme cells, strain up to 100 % are obtained before failure.

For the orientation of 45 degrees (Fig. 6(c)), the loading is aligned with one diagonal of the unit cell square. The strain field is then symmetric at the microscopic scale. The shear component of the strain (which is not shown) is negative for the couple of homologous edges of the unit cell (left and right) whereas it is exactly the opposite for the other couple of homologous edges (top and bottom). A shielding effect is also observed in the vertical zones between the holes which are protected from the loading.

For the orientation of 30 degrees (Fig. 6(b)), the loading has no symmetry for the cell square thus the strain field has no symmetry. The shear strain component for the top and bottom edges is higher than for the left and right edges.

Error Fields Obtained by DIC

The correlation error fields (measured at both scales) are plotted in Fig. 7 for the non inclined experiment and for the same load level than Figs. 5 and 6. The grey levels of the images have a dynamic equal to 8 bits ([0 255]) and the error field is plotted in the interval [0 10] grey level. Same levels of errors are obtained for the two others experiments which are not shown. The maximum of the error is concentrated in the vicinity of the holes. The error is higher for the macroscopic DIC than for the microscopic DIC. This is due to the fact that the macroscopic kinematic is not able to capture the heterogeneous strain field in the unit cell. Inside the architectured material, the mean value of the error is similar for both analysis although slightly higher for the macroscopic one : 7 % for the microscopic DIC and 8 % for the macroscopic DIC.

Unit Cell Kinematics

From the analysis presented above, the displacement measured along the boundary of each unit cell is extracted in order to study the unit cell kinematics. The normal displacement field along the edges of this unit cell is fitted (in a least-squares sense) onto a third order polynomial basis:
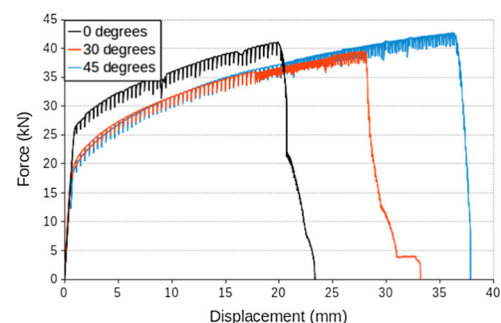
$$u_n = a + bs + cs^2 + ds^3. \tag{9}$$

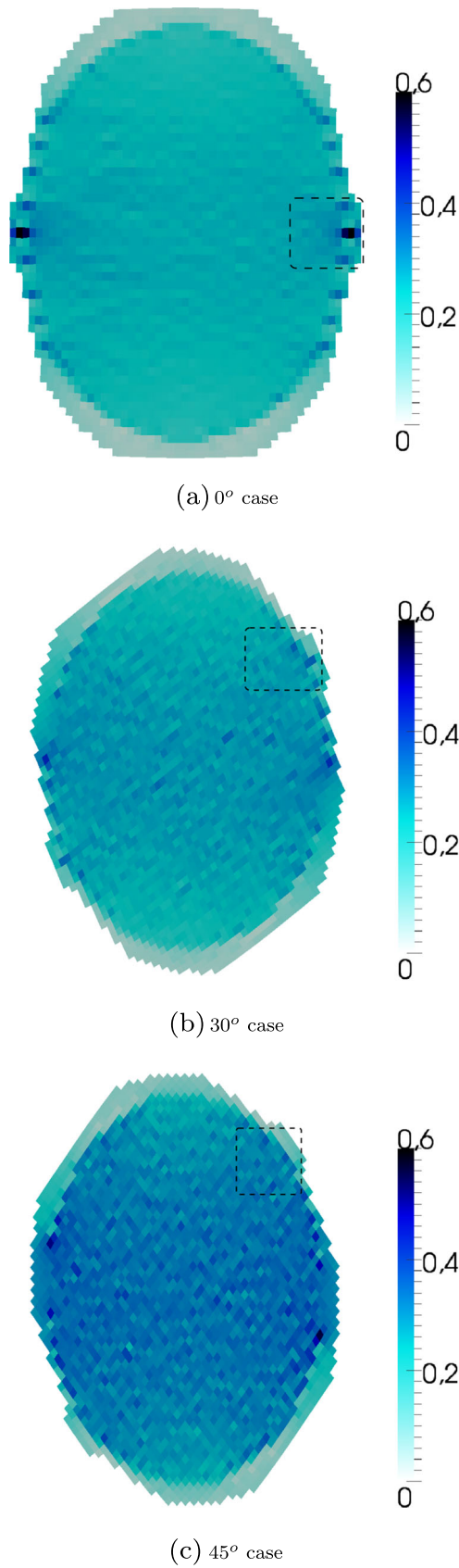**Fig. 4** Load versus displacement curve of the three experiments

(a) 0° case

(b) 30° case

(c) 45° case

Fig. 5 Magnitude of measured Green-Lagrange strain fields at the macroscopic scale for the three experiments

(a) 0° case

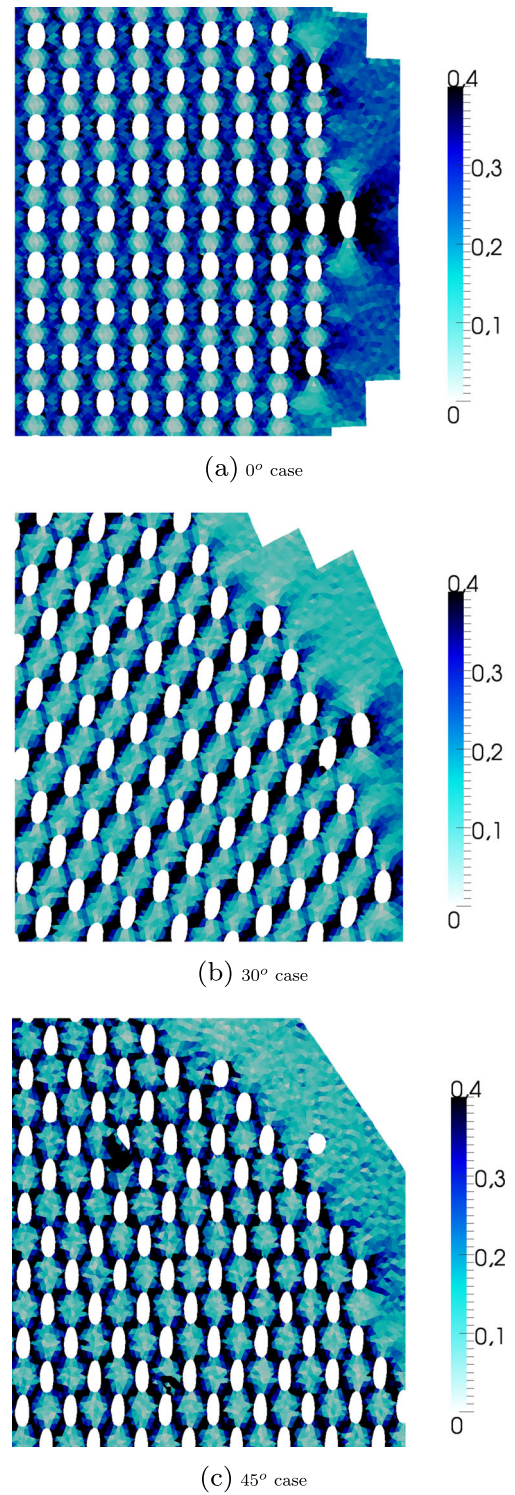(b) 30° case

(c) 45° case

Fig. 6 Magnitude of measured Green-Lagrange strain fields at the microscopic scale for the three experiments

In this equation, s is the curvilinear abscissa along the edge, varying between -1 and 1, and u_n is the displacement normal to the edge. This normal is defined in the frame attached to the unit cell which orientation can be 0,
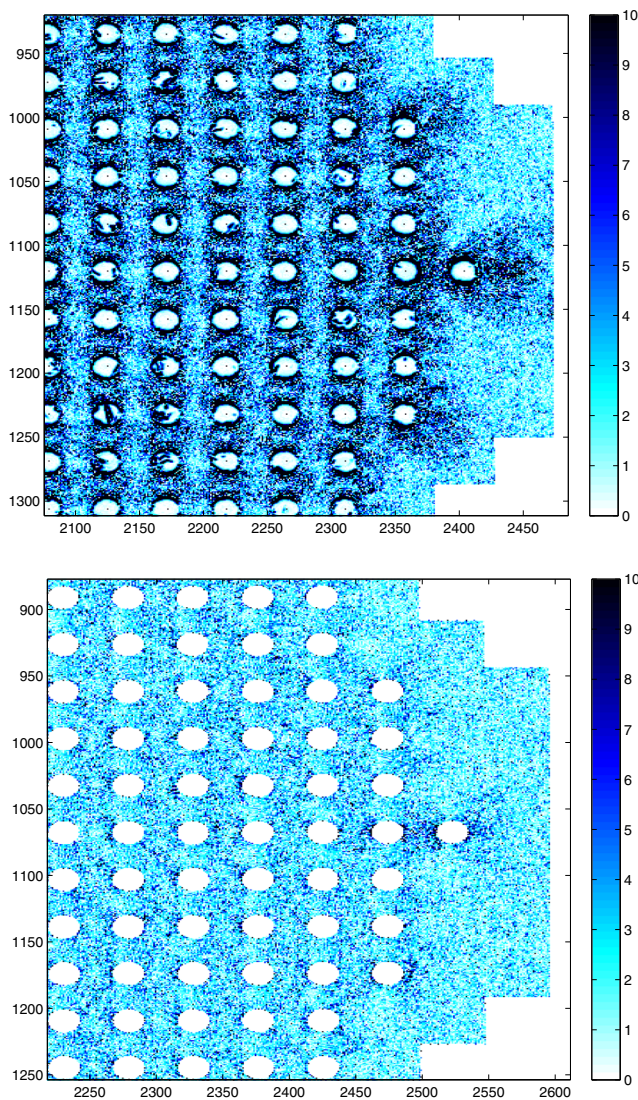
Fig. 7 Magnitude of the error field at the macroscopic (*top*) and the microscopic (*bottom*) scale for the non inclined experiment

30 or 45° as mentioned earlier. Rigid body translations are first extracted then removed from the measured displacement. The resulting displacement field is then projected onto the third order polynomial basis. This choice of third order polynomial basis is due to the different observed deformation patterns and in particular to those resulting from the shear deformation. As illustrated by Fig. 8 varying the orientation of the unit cell network produces different loading of the unit cell with different tension and shear ratios.

The periodicity of the displacement field from one unit cell to the next one will be analyzed from the projected displacements. The transition zone between the homogeneous zone and the central architectured part is studied in a second step. It contains the cells close to the boundary of the architectured material. In the framework of a classical first order periodic homogenization scheme, the displacement on the boundary of the unit cell is written as:

$$\mathbf{u} = \underline{\underline{F}}_M \cdot \mathbf{x} + \mathbf{w}, \tag{10}$$

where $\underline{\underline{F}}_M$ is the transformation gradient at the macroscopic scale, $\mathbf{x}$ is the vector defining the position of the current point along the unit cell boundary and $\mathbf{w}$ is a periodic displacement defined at the microscopic scale. Periodicity conditions for the microscopic displacement $\mathbf{w}$ are defined as:

$$\mathbf{w}_L(s) = \mathbf{w}_R(s) \quad \text{and} \quad \mathbf{w}_T(s) = \mathbf{w}_B(s). \tag{11}$$

where, as defined in Fig. 9, L, B, R, T indices refer to respectively, the left, bottom, right and top edge of the unit cell. Accounting for these periodicity conditions, instead of prescribing the displacement along each edge of the unit cell, the difference between the displacement of opposite edges, for example $\mathbf{u}_T - \mathbf{u}_B$ is defined from the macroscopic transformation gradient:

$$
\begin{aligned}
\mathbf{u}_T - \mathbf{u}_B &= \underline{\underline{F}}_M \cdot (\mathbf{x}_T - \mathbf{x}_B) + \mathbf{w}_T - \mathbf{w}_B \\
&= \underline{\underline{F}}_M \cdot (\mathbf{x}_T - \mathbf{x}_B) \\
&= L \cdot \underline{\underline{F}}_M \cdot \mathbf{N}_T
\end{aligned}
\tag{12}
$$

In the last equation, L is the size of the square unit cell and $\mathbf{N}_T$ is the unit normal of the top edge (combined with the y axis). The same relation holds between right and left edges. From the displacement measurements by DIC, it is possible to extract the constant parameters in equation (9). To check for the periodicity of the deformation pattern of the unit cells the following quantity is computed:

$$
\begin{aligned}
(\mathbf{u}_T - \mathbf{u}_B) \cdot \mathbf{N}_T &= (a_T - a_B) + (b_T - b_B)\, s \\
&\quad + (c_T - c_B)\, s^2 + (d_T - d_B)\, s^3 \\
(\mathbf{u}_R - \mathbf{u}_L) \cdot \mathbf{N}_R &= (a_R - a_L) + (b_R - b_L)\, s \\
&\quad + (c_R - c_L)\, s^2 + (d_R - d_L)\, s^3
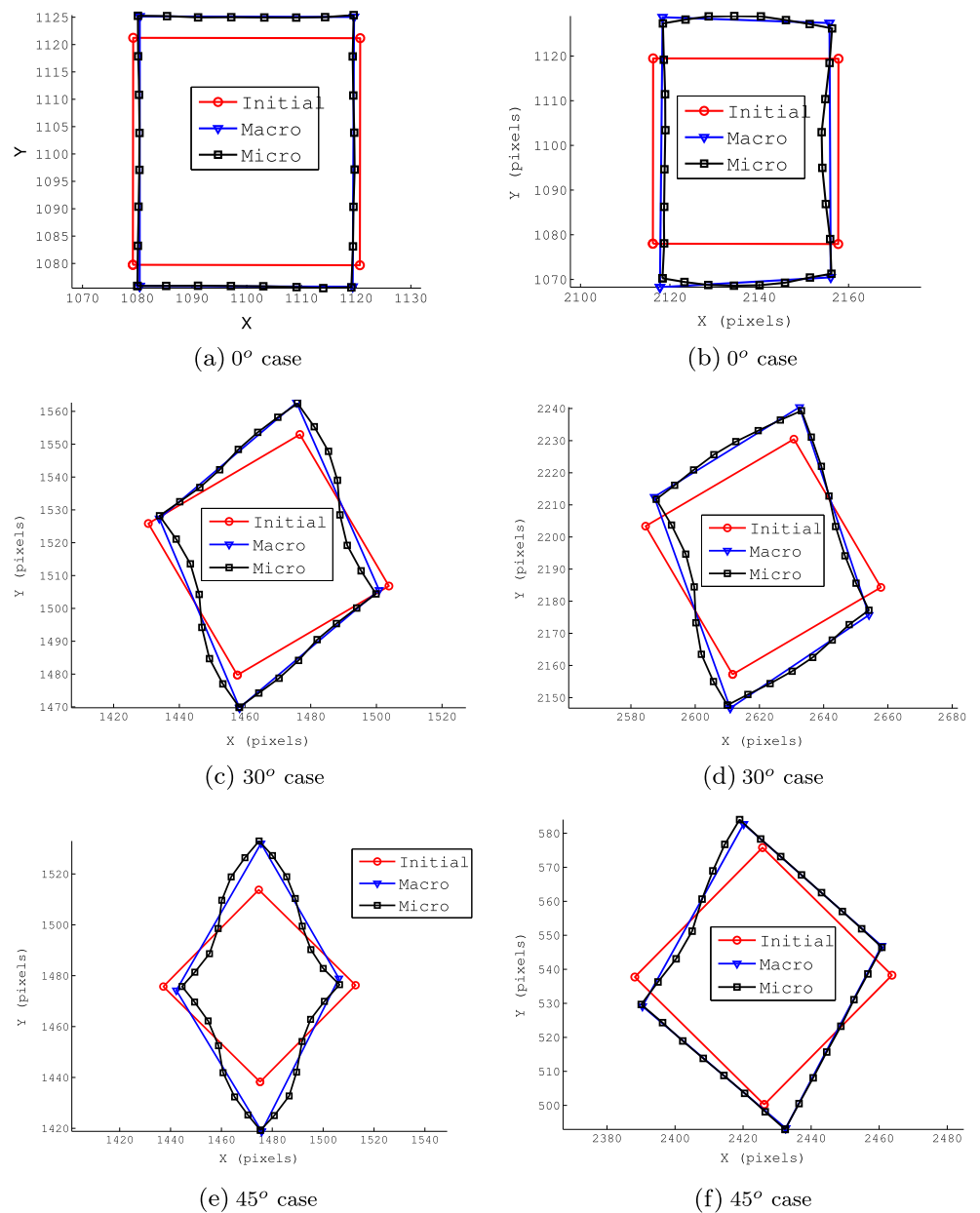\end{aligned}
\tag{13}
$$

In the case of a first order scheme, a unit cell kinematic is periodic if the contribution of the terms in order one (s), two (s^2) and three (s^3) vanish : this means that $b_R - b_L$, $c_R - c_L$ and $d_R - d_L$ as well as the same quantities for top and bottom sides are all close to zero.

Analysis of cell Edges Kinematics

The evolution of the four (a, b, c and d) parameters are plotted as functions of the average mean vertical elongation of the zone of interest and for each of the three experiments (using three different orientations of the unit cell network with respect to the loading axis). Blue curves correspond to the mean value parameters over all the cells and the red curve to the standard deviation of the corresponding parameter. Figures 10 and 11 show the results of the

Fig. 8 (**a**), (**c**) and (**e**) : deformation of the centred unit cell boundary for the three orientations. (**b**), (**d**) and (**f**) : deformation of the unit cell boundary placed at the extreme right of the middle horizontal line for the three orientations. The initial unit cell contour in red is compared to its deformed shape by the macro DIC analysis in blue and the micro DIC analysis in black

(a) 0° case

(b) 0° case

(c) 30° case

(d) 30° case

(e) 45° case

(f) 45° case

top and right edge of the cell, respectively. When the cell network is aligned with the loading direction (0°), cells are mainly loaded in tension along the loading axis. The order 0 parameter is, as expected, predominant for the top edge

(a_T). For the right edge, a_R has a negative mean value corresponding to the Poisson effect due to uniaxial tension. An illustration of the unit cell kinematics is shown in Fig. 8(a).

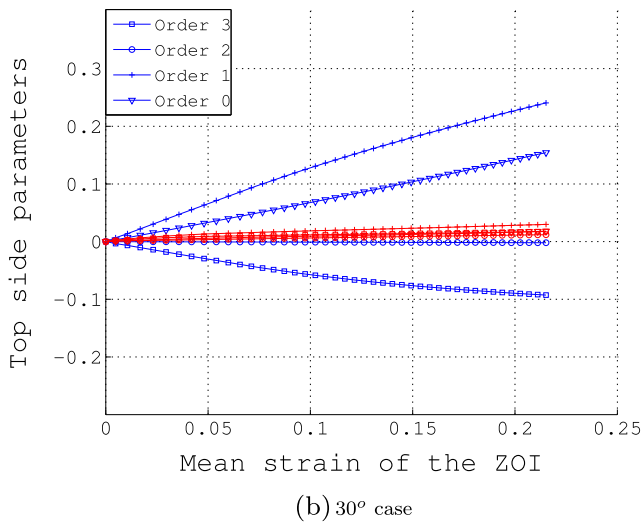**Fig. 9** Schematic picture of the undeformed reference unit cell for each orientation

(a) 0° case

(b) 30° case
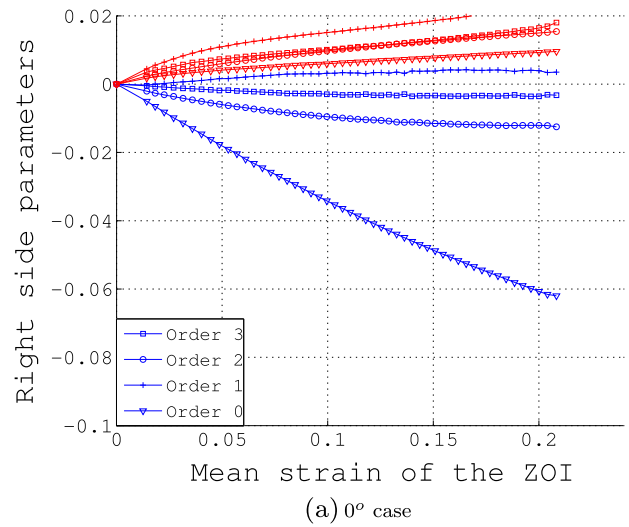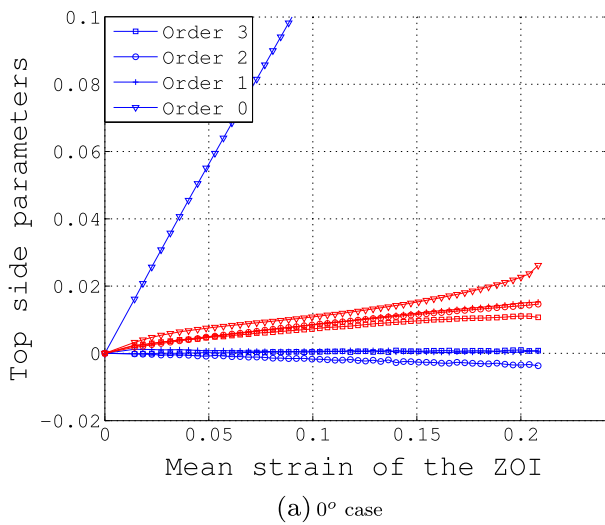
(c) 45° case
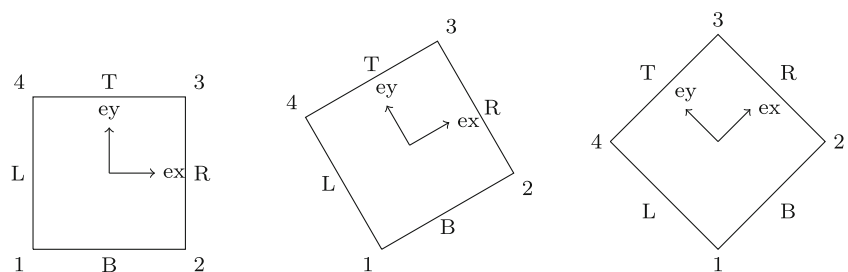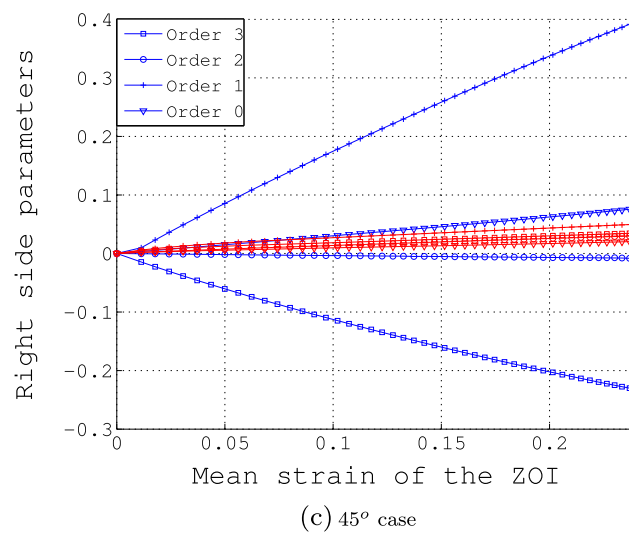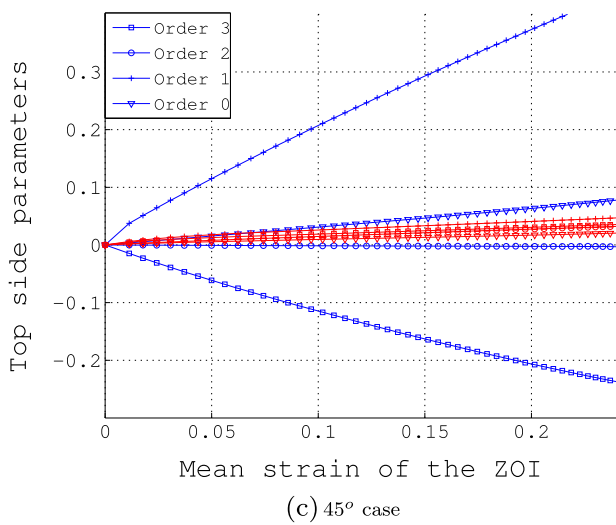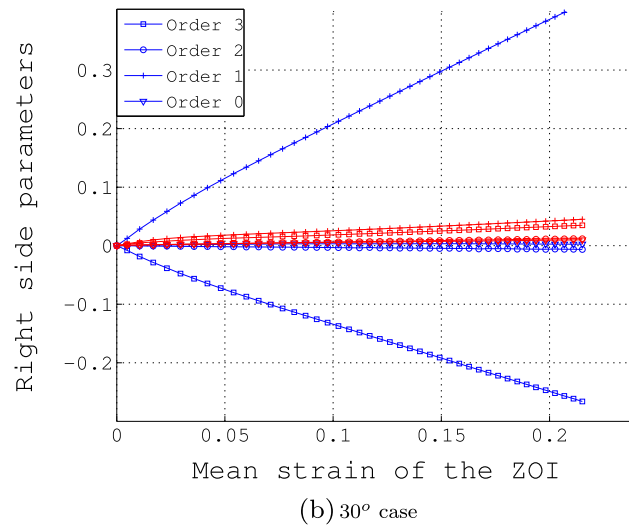
Fig. 10 Evolution of the four kinematic parameters a_T, b_T, c_T and d_T for the three orientations. The mean value (*blue curves*) and the standard deviation (*red curves*) are plotted as functions of the vertical elongation of the ZOI
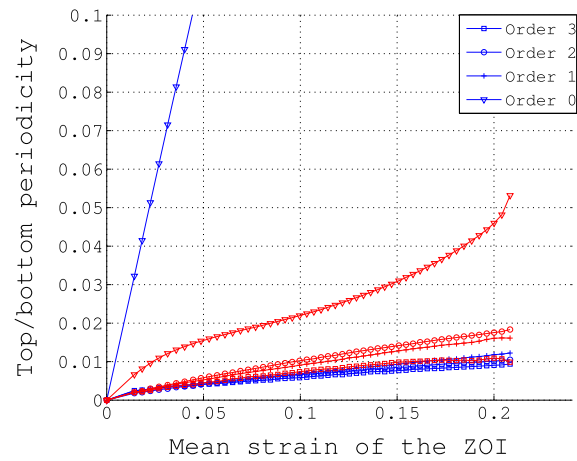

(a) 0° case

(b) 30° case

(c) 45° case

Fig. 11 Evolution of the four kinematic parameters a_R, b_R, c_R and d_R for the three orientations. The mean value (*blue curves*) and the standard deviation (*red curves*) are plotted as functions of the vertical elongation of the ZOI

For the orientation of 30° and 45°, the unit cells are loaded in a mixed tensile/shearing mode as observed in Figs. 10(b) and (c). In the case of 45°, the loading direction is aligned with the diagonal of the initial square unit cell. During the loading, the symmetry is maintained. Indeed, the kinematic parameters of the edge deformation are similar in amplitude for the top edge (Fig. 10(c)) and for the right edge (Fig. 11(c)). It has to be noticed that the dominant term corresponds to the first order. These terms correspond to a rotation of the edges. Order 3 parameter is also predominant compared to the second order. These terms are linked to a shear deformation of the unit cell edges.

In the case of the 30° orientation, the unit cell has no symmetry with respect to the loading axis. Then, the behaviour obtained in Figs. 10(b) and 11(b) is different. However, it is observed that for both cases, the dominant terms are order 1 and 3. The first term is related to a rotation of the edges whereas order 3 corresponds to shear deformations. One can remark that the mean value of order 3 is larger for the right side than for the top side which is illustrated in the Fig. 8(c) The top edge kinematic has also a significant order 0 contribution. This contribution is smaller for the right edge because their normals are nearly orthogonal to the loading direction.
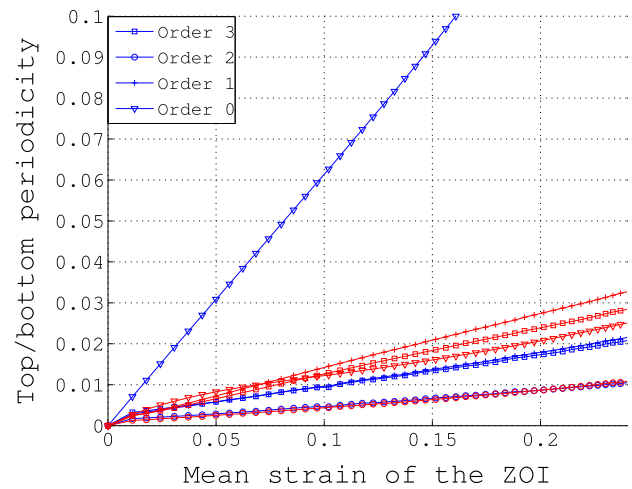
Periodicity

The fitting parameters are now extracted for the four edges of each unit cell. The difference between the parameters extracted for the right and left edges, respectively top and bottom, are then computed. As illustrated by equation (13), this allows for studying the periodicity and the contribution of the macroscopic deformation gradient to the unit cell kinematics. The evolution of the four parameters are plotted in Fig. 12 for the three orientations of the hole network and for the top/bottom difference. For the top/bottom case dominant terms are order 0. The mean values of the three other parameters are of the same order of magnitude as their standard deviation, meaning that no relevant information can be extracted. Fig. 13 shows the results for the left/right periodicity analysis. As for top/bottom couple, the term of order 0 is dominant. Only for the 30° case (Fig. 13(b)) the four terms are negligible. This analysis confirms that the unit cell edges deformation is due to a constant macroscopic strain gradient and a periodic displacement field accommodating locally the effect of unit cell heterogeneity. This property is well established for a linear behaviour of the material within the cell. This experimental result confirms that for this type of microstructure and this type of material first order periodic homogenization can be also used for large plastic strains.

(a) 0° case

(b) 30° case
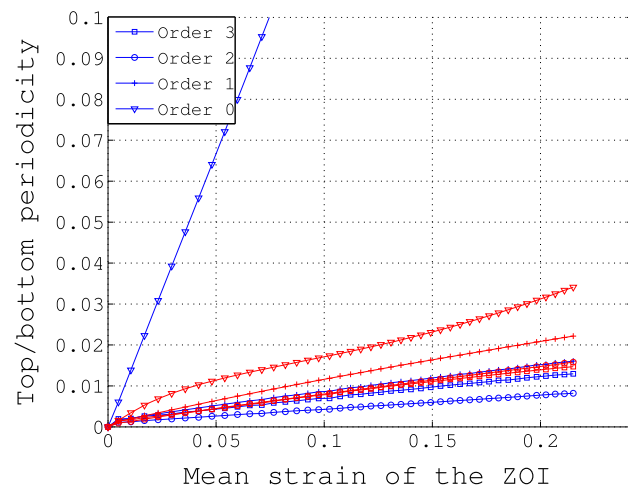
(c) 45° case

Fig. 12 Evolution of the top/bottom periodicity for the four kinematic parameters. For the three orientations, the mean value (*in blue*) and the standard deviation (*in red*) are plotted as functions of the vertical elongation of the ZOI
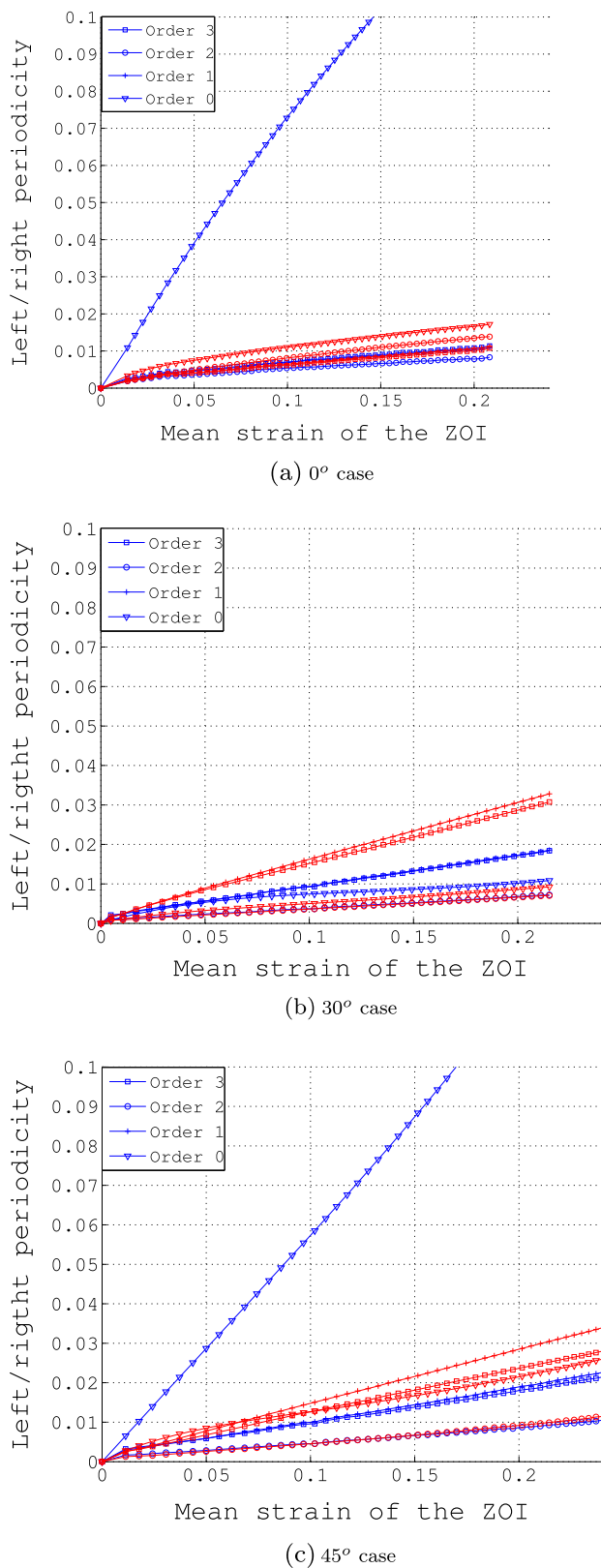
(a) 0° case

(b) 30° case

(c) 45° case

Fig. 13 Evolution of the top/bottom periodicity for the four kinematic parameters. For the three orientations, the mean value (*in blue*) and the standard deviation (*in red*) are plotted as functions of the vertical elongation of the ZOI

Homogenized Microscopic *v.s.* Macroscopic Strain

Using the observation of preceding section, one may extract the homogenized macroscopic strain ε^m which is applied to the unit cells. For the 0 degree case and for the group of 5x5 unit cells located in the center of the specimen, this measure is obtained from:

$$\varepsilon_{11}^m = \frac{a_R - a_L}{2} \quad \text{and} \quad \varepsilon_{22}^m = \frac{a_T - a_B}{2}. \tag{14}$$

This strain measure is compared to the macroscopic strain ε^M obtained from the DIC at the macroscopic scale, *i.e.* using a mesh with one quadrangular element per unit cell. The longitudinal and the transverse components of these strain tensors are respectively plotted in Fig. 14(a) for the 0° case. In this case the longitudinal component of the strain tensor is along the loading direction and the transverse strain component is orthogonal to the loading direction.

For the two other cases, it is chosen to plot the longitudinal and transverse strains in the coordinate frame associated with the unit cell as defined in Fig. 9. In Figs. 14(b) and (c) are respectively reported the results of the longitudinal and transverse components for the 30° and 45° cases.

A good agreement between the two macroscopic strain measures is obtained with a scatter of 1.5 % in average (for the 0° case). It is thus shown that the macroscopic strain extracted from the microscopic displacement measurement is consistent with the direct measurement of the macroscopic strain.

Non Periodic Unit Cells

Beside this mean behaviour, we will now try to investigate the non periodic effects. A cell is considered to have a non periodic behaviour, if one of the four periodicity parameters (plotted in Figs. 12 and 13) has value outside the range defined by the mean parameter value ± 1.5 times its standard deviation. We will now illustrate the relative importance of these non periodic cells. The standard deviation of the periodicity parameters is now computed ignoring these cells. The results are shown for the three orientation cases and top/bottom periodicity in Fig. 15, respectively for left/right periodicity in Fig. 16. The evolution of only one parameter is presented for the sake of clarity: the first order parameter for the non inclined experiment, the second order parameter for the 30° case and the third order parameter for the 45° case. The standard deviation for order 1, 2 and 3 is divided by a factor of about 3. The standard deviation of the parameters are now lower than their average, the only non vanishing term being order 0. This means that this set of unit cells (all the cells except those having one of the four periodicity parameters with a value outside the range defined by its
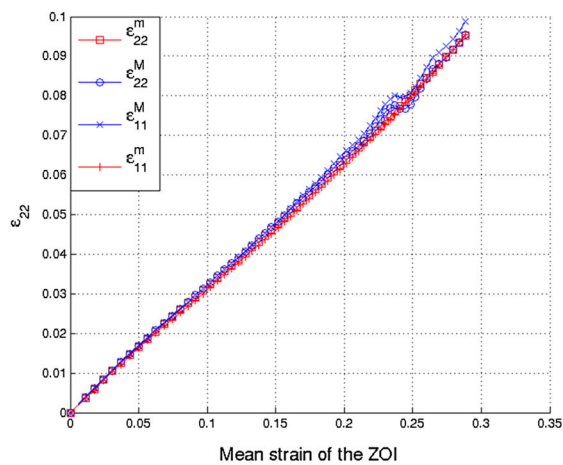
(a) 0° case

(b) 30° case
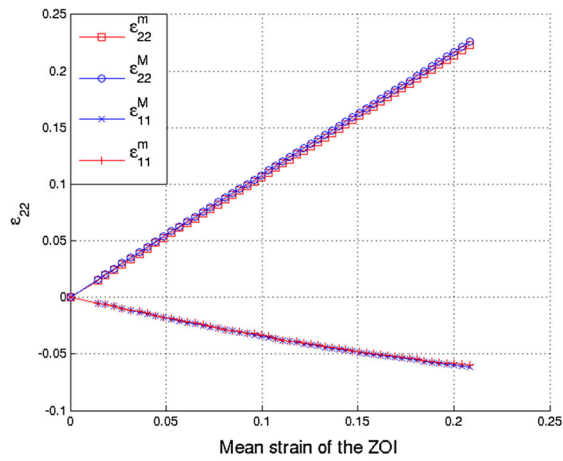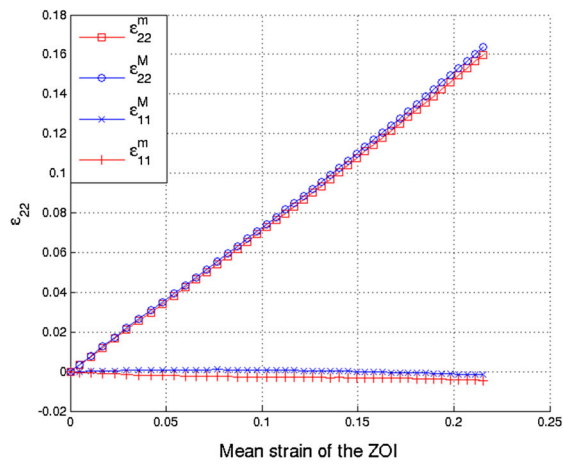
(c) 45° case

Fig. 14 Comparison of the strain measured directly from the macro DIC analysis (in blue) and the strain extracted from the analysis of the deformation of the unit cell boundary in the micro DIC analysis (in red). The longitudinal and transverse components of the strain tensor in the unit cell's coordinate frame are plotted as functions of the vertical elongation of the ZOI for the three cases (0° in (**a**), 30° in (**b**) and 45° in (**c**))
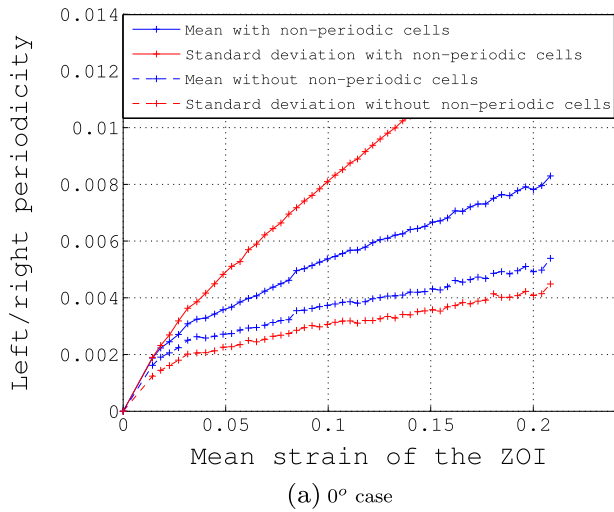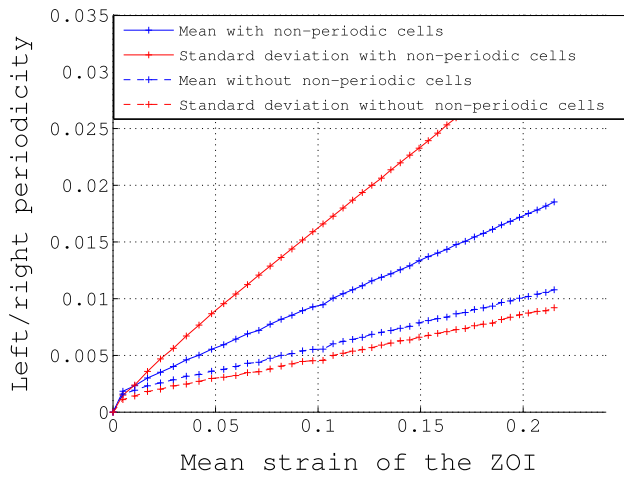

(a) 0° case

(b) 30° case
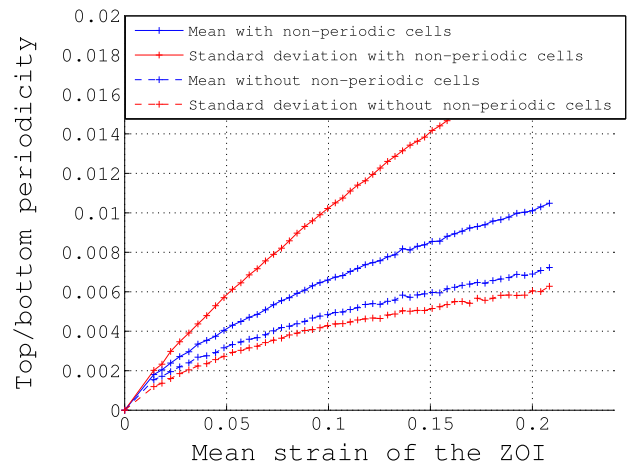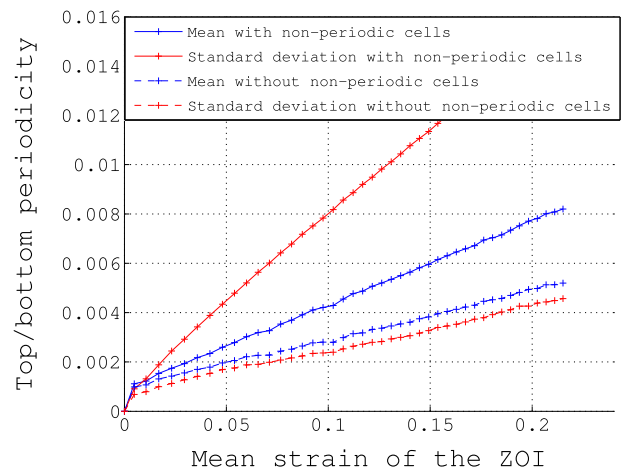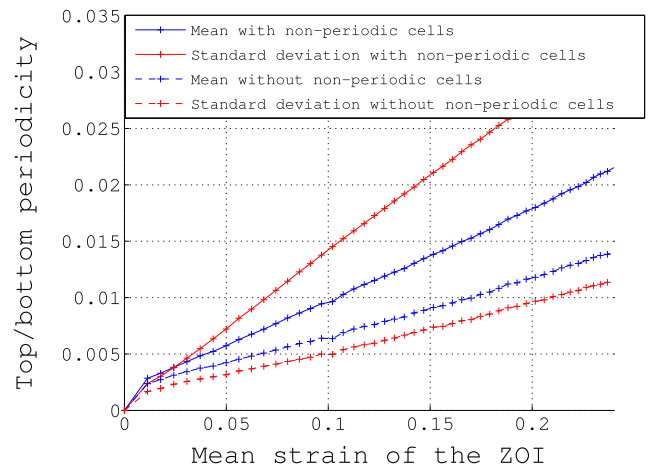
(c) 45° case

Fig. 15 Evolution of the top/bottom periodicity for the second order term of the contour deformation. For the three orientations, the mean value (*in blue*) and the standard deviation (*in red*) with or without excluding cells with non periodic behaviour are plotted as functions of the vertical elongation of the ZOI

(a) 0° case

(b) 30° case

(c) 45° case

Fig. 16 Evolution of the left/right periodicity for the second order term of the contour deformation. For the three orientations, the mean value (*in blue*) and the standard deviation (*in red*) with or without excluding cells with non periodic behaviour are plotted as functions of the vertical elongation of the ZOI
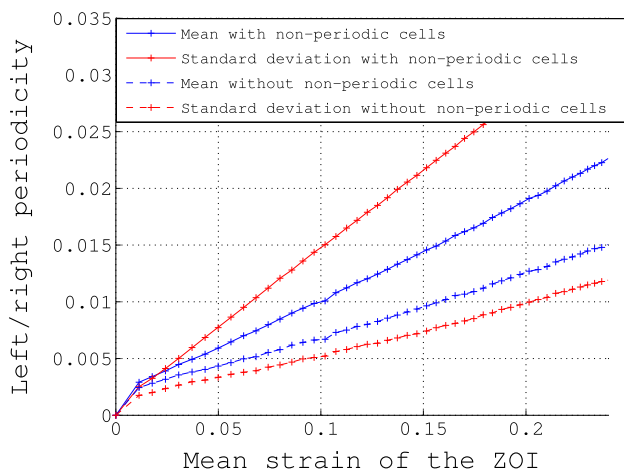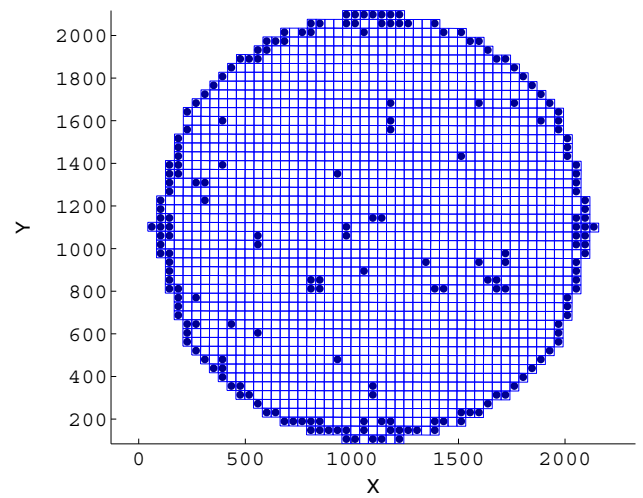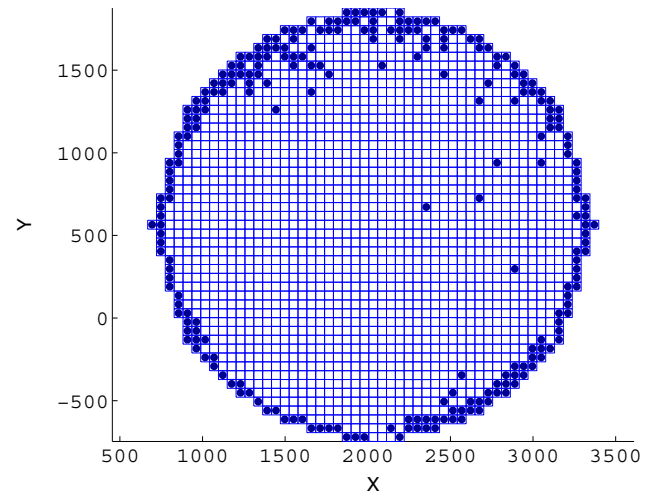

(a) 0° case

(b) 30° case
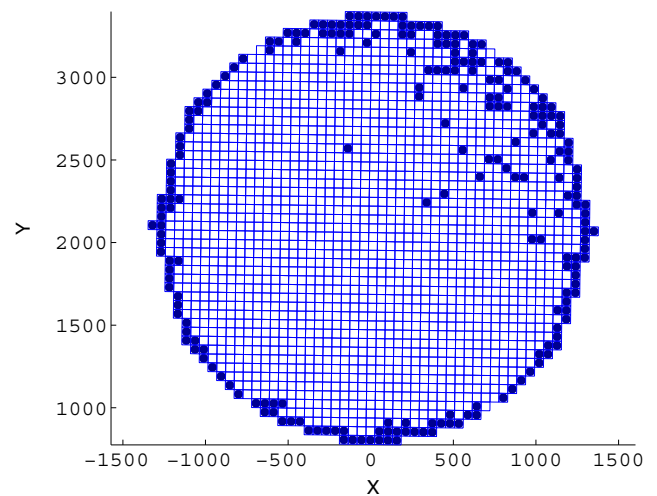
(c) 45° case

Fig. 17 For the three orientations, the cells with non periodic behaviour (top/bottom or left/right) are filled

average ±1.5 times its standard deviation) is submitted to periodic boundary kinematics (see the equation (13)).

Transition Zone Between the Heterogeneous/Homogeneous Material

One shall now investigate the position of these non periodic cells. The cells that have a non periodic behaviour along the top/bottom direction or along the left/right direction are represented with dots where each unit cell is representing by a quadrangle (Fig. 17). All the non periodic cells are located on one row along the boundary of the architectured zone, except for some randomly placed cells in the bulk of the heterogeneous zone. For these cells, non periodicity is due to noisy measurements, all the non periodic cells are located along the boundary of the architectured zone. It may be said that all the cells along the boundary of the architectured zone have a non periodic behaviour regardless of their position and the load orientation. To illustrate non periodic effects, the deformed middle right unit cell is plotted for the three orientations in Figs. 8(b), (d) and (f). This cell has its left edge linked to another unit cell but its three other edges are linked to the homogeneous material. Compared to Fig. 8(c), the deformation of the cell is completely different. Higher order effects are obtained especially for the 0° case. For the 30° and the 45°, the cell is mainly loaded in tension, contrary to the cells in the bulk of the architectured zone which are loaded in both tension and shear due to the lattice orientation with respect to the loading direction. The edges cell kinematics is thus very different.

Conclusions

In this paper, a specimen has been designed in order to analyse the deformation of an architectured material based on a periodic lattice and a square unit cell with a hole. The effect of lattice orientation with respect to the uniaxial loading direction is investigated. The deformation of the specimen is measured by DIC using very high resolution images. These high resolution images enable to perform from a unique data set a two scales DIC analysis of the strain field: one at the microscopic scale giving fine informations within each cell and one at macroscopic scale. From the first analysis, the edges displacement of each cell are analyzed through periodic and non periodic homogenization schemes. The averaged cell strain that is subsequently extracted agrees well with the macroscopic DIC analysis values. A statistical analysis of the cell edges kinematics is carried out. The edges displacement is projected onto a polynomial basis, and their distribution is analysed. It is concluded that the cells edges kinematics fall

within the scope of first order periodic homogenization theory. The non periodic effect are confined to one row of cells along the boundary of the architectured zone. All the cells along this boundary have a non periodic edge kinematics irrespective of the lattice orientation. The analysis has been conducted for a wide range of strain including large plastic deformation. These experimental results give interesting indications for the homogenization strategies to be used in computations in case of large elastoplastic strains.

References

1. Nemat-Nasser S, Hori M (1999) Micromechanics: overall properties of heterogeneous materials. Elsevier, Amsterdam
2. Ponte Castañeda P, Suquet P (1998) Nonlinear composites. Adv Appl Mech 34:171–203
3. Fish J, Shek K, Pandheeradi M, Shephard MS (1997) Computational plasticity for composite structures based on mathematical homogenization: Theory and practice. Comput Methods Appl Mech Eng 148:53–73
4. Feyel F, Chaboche JL (2000) Fe2 multiscale approach for modelling the elastoviscoplastic behaviour of long fibre sic/ti composite materials. Comput Methods Appl Mech Eng 183(3-4):309–330
5. Kouznetsova VG (2002) Computational homogenization for the multi-scale analysis of multi-phase materials. PhD thesis, Technische Universiteit Eindhoven
6. Gitman IM, Askes H, Sluys LJ (2007) Representative volume: Existence and size determination. Eng Fract Mech 74(16):2518–2534
7. Kouznetsova VG, Geers MGD, Brekelmans WAM (2004) Multiscale second-order computational homogenization of multi-phase materials: a nested finite element solution strategy. Comput Methods Appl Mech Eng 193:5525–5550
8. Feyel F (2003) Comput Methods Appl Mech Eng 192(28-30):3233–3244. Multiscale Computational Mechanics for Materials and Structures
9. Coenen EWC, Kouznetsova VG, Geers MGD (2012) Multi scale continuous discontinuous framework for computational homogenization localization. J Mech Phys Solids 60 (8):1486–1507
10. Kaczmarczyk L, Pearce CJ, Bićanić N (2008) Scale transition and enforcement of rve boundary conditions in second-order computational homogenization. Int J Numer Methods Eng 74:506–522
11. Ghahremaninezhad A, Ravi-Chandar K (2012) Ductile failure behavior of polycrystalline al 6061-t6. Int J Fract 174 (2):177–202
12. Passieux J-C, Bugarin F, David C, Périé J-N, correlation L. Robert. Multiscaledisplacementfieldmeasurementusingdigitalimage (2014) Application to the identification of elastic properties. Exp Mech:1–17
13. Weck A, Wilkinson DS (2008) Experimental investigation of void coalescence in metallic sheets containing laser drilled holes. Acta Mater 56(8):1774–1784
14. Sutton MA, Wolters WJ, Peters WH, Ranson WF, McNeill SR (1983) Determination of displacements using an improved digital correlation method. Image Vis Comput 1 (3):133–139

15. Besnard G, Hild F, Roux S (2006) Finite-element displacement fields analysis from digital images: Application to portevin le chatelier bands. Exp Mech 46 (6):789–803

16. Hild F, Roux S, Gras R, Guerrero N, Marante ME, Flórez-López J (2009) Displacement measurement technique for beam kinematics. Opt Lasers Eng 47:495–503

17. Réthoré J, Elguedj T, Simon P, Coret M (2010) On the use of nurbs functions for displacement derivatives measurement by digital image correlation. Exp Mech 50:1099–1116

18. Yang R-C (2014) A regularized finite-element digital image correlation for irregular displacement field. Opt Lasers Eng 56(0): 67–73

19. Leclerc H, Périé J-N, Hild F, Roux S (2012) Digital volume correlation: what are the limits to the spatial resolution? Mech Ind 1:361–371

20. Réthoré J, Muhibullah T. Elguedj, Coret M, Chaudet P, Combescure A (2013) Robust identification of elasto-plastic constitutive law parameters from digital images using 3d kinematics. Int J Solids Struct 50(1):73–85